LETTER

doi:10.1038/nature14563

# Quantum-dot-in-perovskite solids

Zhijun Ning[1]†*, Xiwen Gong[1]*, Riccardo Comin[1]*, Grant Walters[1], Fengjia Fan[1], Oleksandr Voznyy[1], Emre Yassitepe[1], Andrei Buin[1], Sjoerd Hoogland[1] & Edward H. Sargent[1]

**Heteroepitaxy—atomically aligned growth of a crystalline film atop a different crystalline substrate—is the basis of electrically driven lasers, multijunction solar cells, and blue-light-emitting diodes[1–5]. Crystalline coherence is preserved even when atomic identity is modulated, a fact that is the critical enabler of quantum wells, wires, and dots[6–10]. The interfacial quality achieved as a result of heteroepitaxial growth allows new combinations of materials with complementary properties, which enables the design and realization of functionalities that are not available in the single-phase constituents. Here we show that organohalide perovskites and preformed colloidal quantum dots, combined in the solution phase, produce epitaxially aligned 'dots-in-a-matrix' crystals. Using transmission electron microscopy and electron diffraction, we reveal heterocrystals as large as about 60 nanometres and containing at least 20 mutually aligned dots that inherit the crystalline orientation of the perovskite matrix. The heterocrystals exhibit remarkable optoelectronic properties that are traceable to their atom-scale crystalline coherence: photoelectrons and holes generated in the larger-bandgap perovskites are transferred with 80% efficiency to become excitons in the quantum dot nanocrystals, which exploit the excellent photocarrier diffusion of perovskites to produce bright-light emission from infrared-bandgap quantum-tuned materials. By combining the electrical transport properties of the perovskite matrix with the high radiative efficiency of the quantum dots, we engineer a new platform to advance solution-processed infrared optoelectronics.**

Heteroepitaxy has so far largely relied on vacuum methods such as molecular-beam epitaxy, atomic-layer epitaxy, and metallo-organic vapour-phase epitaxy[1,2]. These methods have been used to test and refine theoretical predictions of the conditions under which crystalline coherence is preserved even in the presence of a mismatch in the native lattices (strained-layer epitaxy). The result is a vast body of theory, knowledge, and practice regarding vapour-phase epitaxy. Since interfacial defects are rare at suitably designed hetero-interfaces, highly efficient luminescent materials have been created that have enabled efficient electrically injected lasers and light-emitting diodes for fibre-optic communications and high-efficiency lighting[3–5].

The past two decades have seen the rapid rise of soft condensed matter, often in the form of solution-processed semiconductors based on organic molecules, polymers, and colloidal nanoparticles (plates, wires, and dots)[6–10]. At the same time, bulk organohalide semiconductor perovskites that exhibit large and perfect crystalline domains have improved in size, properties, and performance. These materials have enabled the development of the perovskite solar cell[11–13].

We investigated whether, under the right conditions, heteroepitaxial alignment could be produced between bulk perovskite semiconductors and quantum-tuned nanoparticles. Thin films consisting of multi-material, yet internally epitaxially aligned, heterocrystals—complex crystals we term poly-heterocrystalline (PHC) solids—could perhaps combine, without undue photocarrier loss, the desired properties of each phase: the excellent charge carrier transport properties of the bulk perovskites, and the quantum-tuned infrared luminescence of the quantum-dot phase.

Solution processing is one approach to the application of organic perovskites. For example, methylammonium lead iodide perovskite ($MAPbI_3$) has led to the most efficient solution-processed solar cells reported so far. And, colloidal quantum dots (CQDs) based on PbS exhibit highly tunable photophysical properties, including in the near- and short-wavelength infrared, which the perovskites have so far failed to access. In terms of compatibility, $MAPbI_3$ and PbS possess related crystal structures (tetragonal and rock-salt, respectively), each having a six-coordinated Pb atom, and with Pb–Pb distances ($MAPbI_3$, 6.26 Å; PbS, 5.97 Å) that are within 4.6% of one another[11].

Consequently, we proposed that, if formed from a mixed solution phase into a solid phase (Fig. 1), then these two materials could potentially form PHC solids exhibiting optoelectronic properties that take advantage of the best features of each. Structurally, the PbS-CQD lattice matches well with the perovskite structure both three-dimensionally (Fig. 1a) and two-dimensionally (Fig. 1b). Studies have previously elucidated the synthesis and properties of composite organic/inorganic crystalline hybrids[14]; here we aim to engineer a heterocrystalline solid-state solution between two different, but structurally affine, materials. Specifically, we aim to combine the strong luminescent efficiency of the quantum dots with long-range carrier transport in the perovskite matrix.

To implement atomic-level coherence between the inorganic PbS and the organometallic $MAPbI_3$ phase, we require an organic-ligand-free strategy to cap the PbS nanoparticles. Colloids have recently been synthesized that were stabilized not using traditional aliphatic ligands, but rather using halide ligands that were introduced from the perovskite precursor methylammonium iodide[15,16]. We use this method to prepare our CQDs.

Structural affinity is necessary but not sufficient to produce epitaxial bonding between the two phases; energetic considerations must also be taken into account. Here we use density functional theory (DFT) to study the interface-formation energy between the PbS (100) plane and the perovskite (110) plane (Extended Data Fig. 1)[17]. The interfacial energy is less than 10 meV $Å^{-2}$, suggesting that the growth of perovskite on PbS at room temperature is nearly as feasible as homoepitaxy of PbS on PbS or perovskite on perovskite. DFT further reveals that the epitaxial three-dimensional embedding of PbS CQDs inside a perovskite matrix is achieved without the formation of interfacial defects (Fig. 1c, d); that is, the bandgap is predicted to remain open, with no in-gap defects predicted (Extended Data Fig. 2).

We produced a PHC solid as follows. We first exchanged the organic ligands on the PbS CQDs for short halide (iodide in this case) anionic ligands (Extended Data Fig. 3a). We then mixed these inorganically terminated CQDs with $PbI_2$ dissolved in butylamine; this solvent strategy is crucial to maintaining passivation of the CQD surface following film growth. Since $PbI_2$ forms a complex with iodide and binds to the CQD surface, $PbI_2$ and CQDs were, as expected, able to mix in solution. (Transmittance spectra of the colloid showed no loss

[1]Department of Electrical and Computer Engineering, University of Toronto, 35 St George Street, Toronto, Ontario M5S 1A4, Canada. †Present address: School of Physical Science and Technology, ShanghaiTech University, Haike Road 100, 201210 Shanghai, China.
*These authors contributed equally to this work.

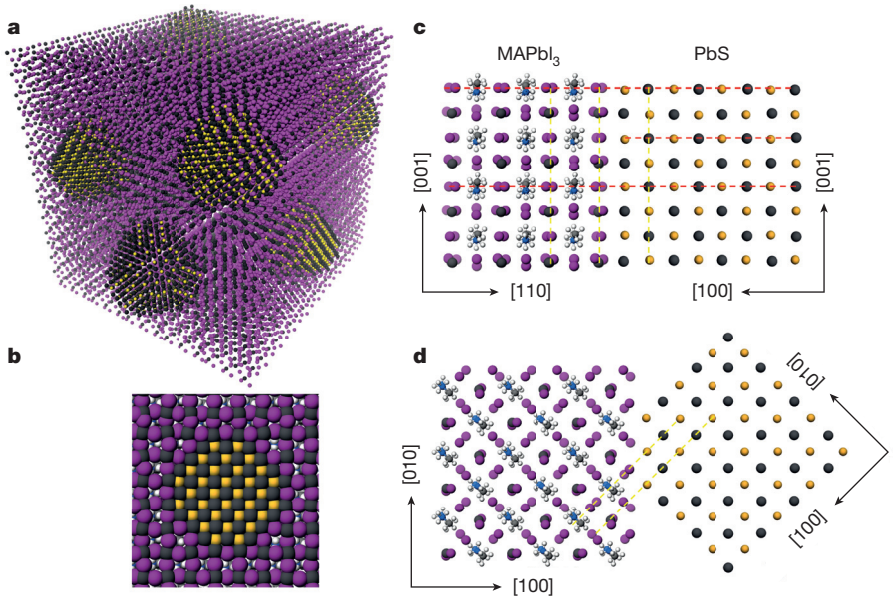


**Figure 1 | Theoretical model of perovskite epitaxial growth on CQDs.** **a**, Three-dimensional atomistic model of CQDs in a perovskite matrix. **b**, Cross-section (two-dimensional view) of a single CQD in perovskite. Here and in **c**, **d**, colours represent the following: grey, lead; purple, iodine; yellow, sulfur. All facets of CQDs match well with perovskite. **c**, **d**, Modelling of PbS and $MAPbI_3$ crystal structure and their interface, showing that perovskite matches well with PbS in both the *X*–*Z* plane (**c**) and the *X*–*Y* plane (**d**). The red dashes show the unit cell size; the yellow dashes are guides to the eye for matching planes.

of optical transmission for photon energies below the CQD bandgap, indicating no increase in scattering and thus no appreciable solution-phase aggregate formation.) By controlling the ratio of $PbI_2$ and CQDs, we tuned the nominal CQD concentration—hereafter expressed as the ratio of CQD to total volume—across the range 0.2–29% (see Extended Data Table 1a for a full list of values used). To fabricate the CQD–$MAPbI_3$ films (Extended Data Fig. 3b, c), we used a previously established sequential (two-step) method[11], whereby the $PbI_2$–CQD films are initially deposited via spin-coating onto a glass substrate, and are then soaked in a $CH_3NH_3I$/isopropanol solution. X-ray photoelectron spectroscopy (XPS) and Rutherford backscattering spectroscopy (RBS) were used to confirm the presence of both PbS and $MAPbI_3$ in the final film (Extended Data Fig. 4a–d). We detected no trace of amine ligands associated with the solvent (Extended Data Fig. 4e). RBS (Extended Data Fig. 4f) was used to estimate the CQD volume percentage as a function of nominal CQD:$MAPbI_3$ ratio.

High-resolution transmission electron microscopy (HRTEM) was used to characterize the crystal structure and orientation of both CQDs and perovskite matrix for a sample with a nominal CQD volume percentage of 4%. Since $MAPbI_3$ is an organic/inorganic hybrid material with lower density than PbS, it has much lower contrast than do inorganic CQDs, which facilitates differentiation between the perovskite and PbS phases. The higher contrast of CQDs was confirmed using high-angle annular dark-field scanning transmission electron

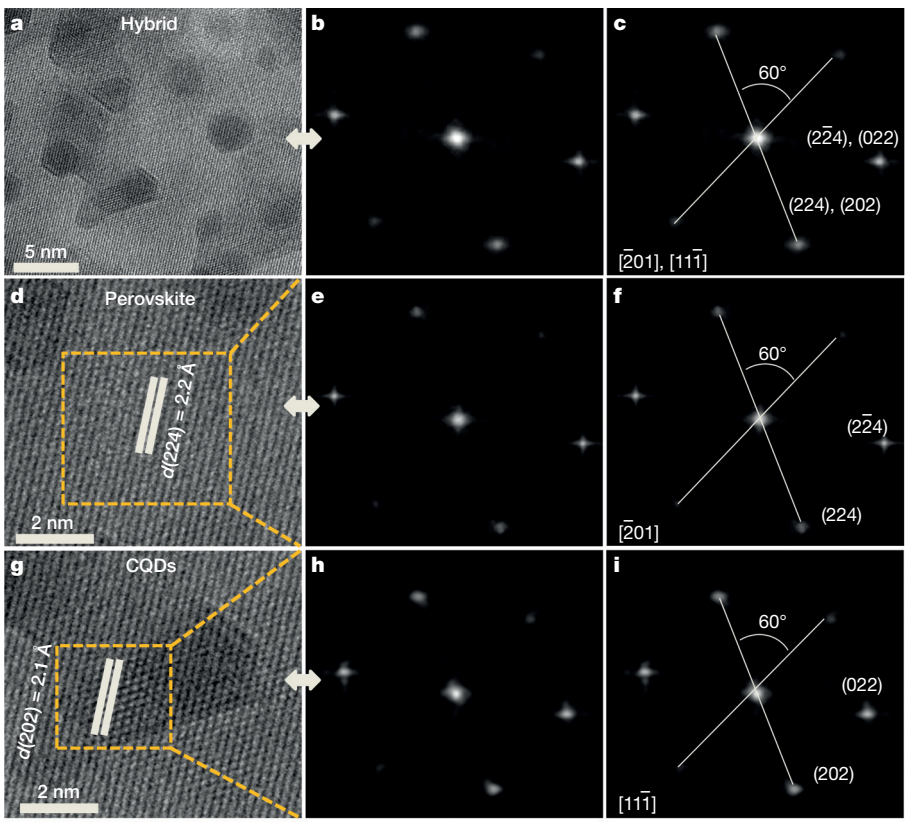


**Figure 2 | HRTEM images and their FFTs.** **a**–**c**, CQD–perovskite hybrid (CQD volume percentage is 3.9%); **d**–**f**, perovskite ($MAPbI_3$); **g**–**i**, CQDs. Images in **b**, **e**, and **h** are FFTs of the HRTEM images shown in **a**, and the yellow boxed regions in **d**, and **g**, respectively, and are the same as those in **c**, **f**, and **i**, but without the overlaid text. For perovskite, the lattice fringes are indexed to the (224) planes. For the CQDs, the lattice fringes are indexed to the (022) planes. In real space, the *d*-spacing value of the (224) plane of perovskite ($d(224) = 2.2$ Å) matches well with that of the (202) plane of PbS ($d(202) = 2.1$ Å). This is consistent with the modelling, which shows that the (100) plane of PbS matches well with the (110) plane of perovskite. The FFT images in **f** and **i** show the same intersection angles (60°) for perovskite (between the (2$\bar{2}$4) and (224) planes) and CQDs (between the (022) and (202) planes), indicating that they match not only two dimensionally, but also three dimensionally, which confirms that the perovskite and the CQDs have the same orientation. Adjustments of the brightness and contrast have been made to the FFT images for ease of visualization.

microscopy (HAADF-STEM), a direct probe of density variations in the material (Extended Data Fig. 5, Methods). The contrast between CQDs and perovskite is clearly observed in the large field-of-view HRTEM map of Fig. 2a; Fig. 2b shows the corresponding fast Fourier transform (FFT), with lattice planes indexed as indicated in Fig. 2c. The contributions from the perovskite matrix and the quantum dots are distinguished by analysing the subregions shown in Fig. 2d, g for the perovskite and quantum dots, respectively. Well defined lattice fringes with 2.2 Å separation (Fig. 2d) are indexed to the (224) plane of the matrix, as confirmed by the corresponding FFT images (Fig. 2e, f), which show that the real-space HRTEM image is projected along the $[\bar{2}01]$ zone axis. We also measured the lattice fringes of the CQDs, which show the same orientation and are indexed as the (022) plane of PbS (2.1 Å, Fig. 2g–i). This is consistent with simulations that show that the (100) facet of PbS matches well with the (110) facet of perovskite. As demonstrated by the FFT, the angles between $(2\bar{2}4)$ and $[\bar{2}01]$ of perovskite are the same as between (022) and $[11\bar{1}]$ of PbS. Hence, the orientation relationships between $MAPbI_3$ and CQDs are identified: $(022)_{PbS} \| (2\bar{2}4)_{MAPbI_3}$; $[11\bar{1}]_{PbS} \| [\bar{2}01]_{MAPbI_3}$. From this we conclude that the matrix and CQDs have the same orientation, which is observed in real-space microscope images and confirmed using a FFT. This analysis demonstrates epitaxial alignment between perovskite and CQDs. Even a slight misalignment would be revealed by the experimental maps, as suggested by transmission electron microscopy (TEM) simulations of epitaxially oriented versus epitaxially misoriented PHCs (Extended Data Fig. 3d, e)[18].

The optical-absorption spectra for pure CQD films and the new 'dot-in-perovskite' (hybrid) PHCs are shown in Fig. 3a. (Absorption and emission spectra for pure CQD and pure perovskite films are also reported in Extended Data Fig. 6a, b.) Absorption signatures corresponding to each constituent, perovskite and CQDs, are apparent in the hybrid films (Fig. 3a). The photoluminescence spectra are very similar to those of CQDs in film (Fig. 3b), indicating that the photophysical properties of CQDs are kept intact when they are incorporated into the perovskite matrix. As the CQD concentration increases, the absorption spectrum redshifts, consistent with increased inter-dot interaction (potentially partial dot fusion at these high concentrations), which reduces the extent of quantum confinement and thus shrinks the bandgap. This shrinking of the bandgap affects absorption and luminescence to the same extent; it does not, to leading order, impact the Stokes shift. A second effect of increased CQD concentration is increased long-range excitonic and carrier transport from dot to dot,

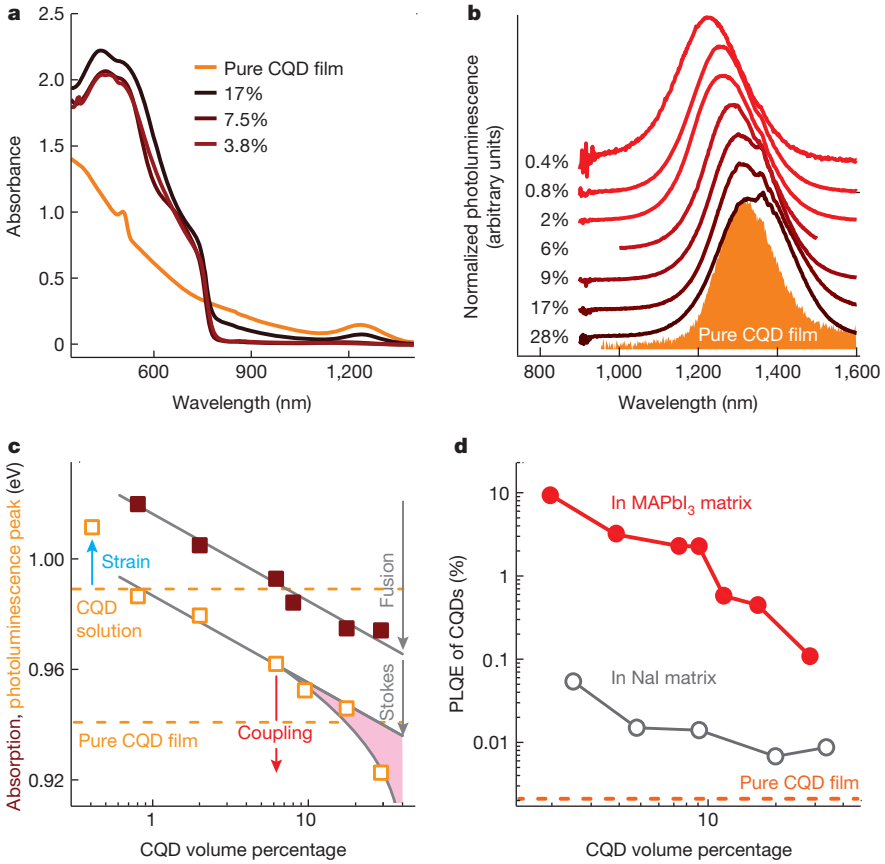


**Figure 3 | Photophysical response of the CQD–perovskite hybrid.** **a**, **b**, Matrix-tuned absorption (**a**) and photoluminescence (**b**) of the CQD–perovskite hybrid. The different curves correspond to different CQD volume percentages, as labelled. After the growth of perovskite, a representative absorption edge around 770 nm appears, whereas both absorption and photoluminescence CQD exciton peaks are preserved, indicating that the properties of CQDs remain unaltered. **c**, The absorption (red filled squares) and photoluminescence exciton peak positions (orange open squares) for the CQDs as a function of CQD:$MAPbI_3$ ratio (illustrated via the CQD volume percentage). Orange dashed lines mark the photoluminescence emission energy for pure CQD films and solutions. Different mechanisms governing the concentration-dependent absorption and emission are also highlighted: CQD fusion causes a redshift, which increases as CQD loading increases (grey arrow 'Fusion'); inter-dot coupling causes a redshift at high CQD concentrations (pink arrow 'Coupling' and shading); and CQD lattice strain that is driven by epitaxial effects, which only has an effect for low CQD concentrations, causes a blueshift (blue arrow 'Strain'). Grey lines are guides to the eye. The concentration-independent Stokes shift causes a redshift (grey arrow 'Stokes'). **d**, PLQE of CQDs in matrix. For lower CQD concentration the PLQE is increased, indicating that CQDs are well dispersed in the matrix and carrier dissociation between CQDs is blocked. In the $MAPbI_3$ matrix, the PLQE is two orders of magnitude higher than that in a NaI matrix, which reveals that a lattice-mismatched matrix (8.8% mismatch for NaI) cannot grow on PbS. This finding confirms that epitaxial growth of matrix on CQDs is critical for CQD surface passivation. The PLQE of a solution-exchanged CQD film (orange dashed line) is shown for comparison. The PLQE of CQDs in the $MAPbI_3$ matrix is approximately 3,000 times greater than in the CQD film.

which is present only at the highest concentrations of CQDs. Through this process, excitons and carriers are transferred to the smallest-gap dots in a population whose lowest-lying quantum-confined levels are inhomogeneously broadened. The increased long-range excitonic and carrier transport does not affect absorption, but redshifts the luminescence, and thus increases the Stokes shift[19,20]. In addition to the mechanisms of partial fusion and increased long-range transport that contribute redshifts, a blueshift (even relative to dots in solution) may also be contributed especially at low CQD loading: tensile strain caused by the lattice mismatch between CQDs and the perovskite slightly expands the PbS lattice, leading to an increase in bandgap[21] (Fig. 3c). This tensile strain acts to the same extent on absorption and emission; see also Extended Data Fig. 7a, b and Methods.

We investigated the CQD photoluminescence quantum efficiency (PLQE)—the ratio of the number of emitted and absorbed photons—for a series of samples with different CQD concentrations (expressed as volume percentages). Initially we used an excitation wavelength of 815 nm, which is below the absorption edge of the perovskite (Fig. 3d), to excite the quantum-dot phase directly and exclusively. The PLQE is highest in low-dot-concentration samples, consistent with minimal quenching associated with the dissociation of excitons into free carriers in the neighbouring quantum dots[22]. The PLQE reaches 9.3%, which is two orders of magnitude higher than that in the pure CQD film. As a control to study the importance of lattice matching on photophysical properties, we changed the matrix to sodium iodide (NaI, rock-salt structure with an 8.8% lattice mismatch with PbS): the PLQE of CQDs in a NaI matrix is almost two orders of magnitude lower than it is in a perovskite matrix (Fig. 3d).

To elucidate the physical origins of enhanced PLQE for dots embedded in a perovskite matrix, we used DFT to investigate whether CQD surfaces can in principle be passivated using the perovskite matrix. Both the highest occupied molecular orbital (HOMO) and the lowest unoccupied molecular orbital (LUMO) are located in the core of PbS CQDs, and the bandgap is trap free. In contrast, for a CQD that is misaligned with the perovskite matrix, trap states are induced at the CQD surface, mostly on the conduction-band side (Extended Data Fig. 2c, d, f).

In addition to providing passivation, the matrix–dot interface is the critical enabler of any charge carrier injection into the CQDs. To study carrier transfer across this interface, we relied on CQDs that are approximately 4 nm in diameter (bandgap of 1 eV) whose LUMO energy level is predicted to lie below the conduction band of the perovskite and whose HOMO energy level should reside above the valence-band edge of the perovskite (Fig. 4a).

By generating excitons in the CQDs only (via photoexcitation using photon energies lower than the perovskite bandgap), and in separate studies where we photogenerate principally in the perovskite matrix, we investigate carrier transfer to, and across, the CQD–perovskite interface. Photoluminescence excitation spectra (Fig. 4b) reveal enhanced CQD emission when the perovskite is excited ($\lambda_{excitation} < 780$ nm)[23]. Increased perovskite content drives a higher CQD photoluminescence intensity when the excitation occurs in the perovskite absorption region. This result qualitatively indicates efficient charge diffusion to, and across, the perovskite–CQD interface. Carrier transfer also occurs in other composite nanomaterials[22,24], such as those made up of small-bandgap-CQD inclusions in a large-bandgap-CQD matrix ('dots-in-dots' films); however, we found that the use of a perovskite matrix provided superior passivation of the quantum dot centres, as evidenced by the nearly two orders of magnitude higher PLQE compared to the same dots in a NaI matrix, and by the fivefold increase in carrier lifetime compared to 'dots-in-dots' films (Extended Data Fig. 8a, b).

The signatures of carrier transfer from the matrix to the quantum dots are also evident in the photoluminescence emission from $MAPbI_3$ in PHC films, as a function of CQD volume percentage (Fig. 4c). In particular, for volume percentages greater than 0.4%, we observe a complete quenching of the perovskite photoluminescence signal, consistent with a highly-efficient removal of photogenerated carriers from the matrix and transfer into the dots. At higher CQD concentrations—in the regime of low densities of injected carriers per dot, where

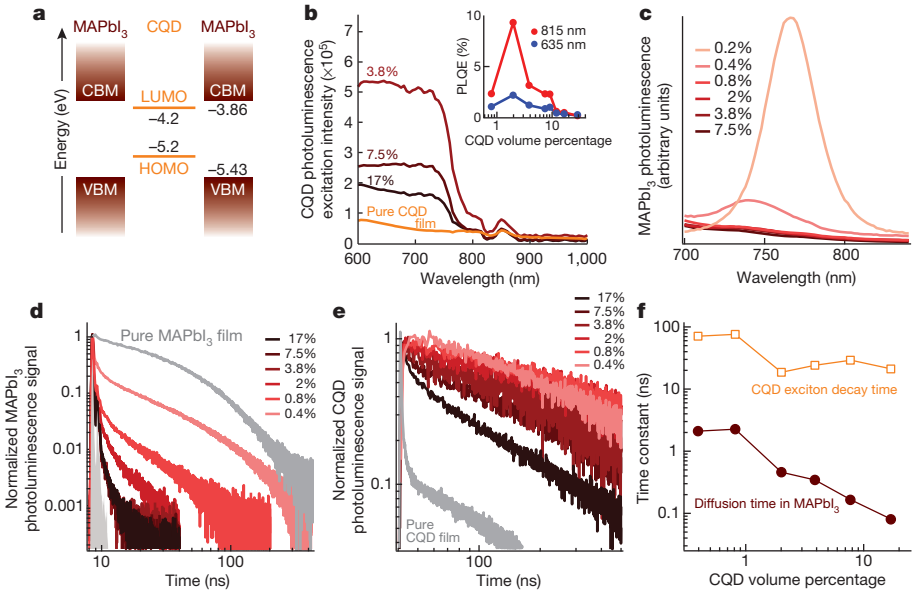


**Figure 4 | Carriers transfer from perovskite to CQDs.** **a**, Electronic band structure of CQDs and perovskite. The LUMO level of CQD is lower than the conduction band minimum (CBM) of perovskite and the HOMO level of CQD is higher than the valence band maximum (VBM) of perovskite, making the transfer of carriers from perovskite to CQDs energetically favoured. **b**, Photoluminescence excitation spectra of CQDs. In the perovskite absorption region ($\lambda$ <780 nm), the photoluminescence excitation intensity increases as perovskite content increases, indicating that carriers excited in perovskite are transferred to CQDs. However, considering the partial carrier loss (via recombination) in perovskite, the PLQE of the hybrid is lower than the internal PLQE of CQD when long excitation wavelength is used (inset). **c**, Photoluminescence spectra of $MAPbI_3$ for PHC films. **d**–**f**, Transient photoluminescence emission from $MAPbI_3$ (**d**) and CQDs (**e**), and corresponding time constants (**f**). As the CQD:$MAPbI_3$ ratio is reduced (the CQD volume percentage decreases), the initial photoluminescence decay time of both perovskite and CQDs becomes longer, as a result of longer transit time in the matrix and reduced carrier dissociation across the CQDs, respectively. The different curves in **b**–**e** correspond to different CQD volume percentages, as labelled.

radiative recombination is dominant over higher-order (for example, Auger) processes—we quantitatively estimate the carrier transfer efficiency from perovskite to CQDs on the basis of photoluminescence and absorption data (Extended Data Table 1b, Methods). The transfer efficiency attains a value exceeding 80% at the highest CQD loading (28% CQD volume percentage).

We investigated the carrier dynamics in the PHC using photoluminescence decay (Fig. 4d, e). We used a two-component decay model to analyse transient photoluminescence. The fast decay that is transient in CQDs is attributed to fast exciton dissociation into neighbouring CQDs, whereas the longer dynamics are ascribed to radiative recombination. The comparison between the PHC and the pure CQD photoluminescence transients in Fig. 4e shows a rapid slowdown of exciton-dissociation dynamics as soon as the CQDs are embedded in the perovskite matrix (from less than 1 ns in pure CQD to 20 ns in PHC at high CQD loading). Furthermore, the fast transient component increases from 20 ns to 70 ns as the CQD concentration is reduced (Fig. 4f) and, correspondingly, the inter-dot separation is increased, consistent with the expected suppression in the exciton-dissociation rate for more isolated dots. The perovskite carrier dynamics (Fig. 4d) show a rapid quenching of the photoluminescence emission, from 25 ns in pure $MAPbI_3$ to about 2 ns in the PHC film at the lowest CQD loading. The photoluminescence lifetime associated with emission from the perovskite phase in 'quantum-dot-in-perovskite' solids is highest (2 ns) at the lowest CQD concentration (Fig. 4f). At this lowest concentration, the inter-dot spacing is an estimated 40 nm, and this relatively larger separation increases the time that is required for photocarriers to diffuse from their point of photogeneration in the perovskite phase to the point of capture into a quantum dot (Extended Data Fig. 9). We use the term 'charge carrier' when referring to photoexcitations in the perovskite phase because prior studies have revealed that photogenerated excitons in perovskite separate to become free carriers within about 2 ps after generation[25]. This analysis does not preclude the possibility that some fraction of excitations could transfer as excitons from perovskite to dot, especially for those excitons that are generated very close to a quantum dot.

This work reports an *in situ* epitaxial growth process of perovskite on quantum-dot surfaces. The quantum dots are effectively passivated by the matrix, without the need for conventional organic ligands, provided lattice-matching conditions are satisfied. The perovskite matrix also provides excellent carrier transport for the CQDs, owing to its superior diffusion length. The present approach paves the way for new strategies to enhance the performance of CQD-based optoelectronic devices, and to extend the spectral diversity of perovskite-based materials towards the infrared.

**Online Content** Methods, along with any additional Extended Data display items and Source Data, are available in the online version of the paper; references unique to these sections appear only in the online paper.

**Received 28 December 2014; accepted 7 May 2015.**


1. Pohl, U. W. *Epitaxy of Semiconductors*: *Introduction to Physical Principles* (Springer, 2013).
2. McCray, W. P. MBE deserves a place in the history books. *Nature Nanotechnol.* **2,** 259–261 (2007).
3. Huang, M. H. *et al.* Room-temperature ultraviolet nanowire nanolasers. *Science* **292,** 1897–1899 (2001).
4. Choi, K., Kako, S., Holmes, M. J., Arita, M. & Arakawa, Y. Strong exciton confinement in site-controlled GaN quantum dots embedded in nanowires. *Appl. Phys. Lett.* **103,** 171907 (2013).
5. Adhikari, H., Marshall, A. F., Chidsey, C. E. D. & McIntyre, P. C. Germanium nanowire epitaxy: shape and orientation control. *Nano Lett.* **6,** 318–323 (2006).
6. Diao, Y. *et al.* Solution coating of large-area organic semiconductor thin films with aligned single-crystalline domains. *Nature Mater.* **12,** 665–671 (2013).
7. Shirasaki, Y., Supran, G. J., Bawendi, M. G. & Bulović, V. Emergence of colloidal quantum-dot light-emitting technologies. *Nature Photon.* **7,** 13–23 (2013).
8. Graetzel, M., Janssen, R. A. J., Mitzi, D. B. & Sargent, E. H. Materials interface engineering for solution-processed photovoltaics. *Nature* **488,** 304–312 (2012).
9. Talapin, D. V., Lee, J., Kovalenko, M. V. & Shevchenko, E. V. Prospects of colloidal nanocrystals for electronic and optoelectronic applications. *Chem. Rev.* **110,** 389–458 (2010).
10. Ma, W., Luther, J. M., Zheng, H., Wu, Y. & Alivisatos, A. P. Photovoltaic devices employing ternary $PbS_xSe_{1-x}$ nanocrystals. *Nano Lett.* **9,** 1699–1703 (2009).
11. Burschka, J. *et al.* Sequential deposition as a route to high-performance perovskite-sensitized solar cells. *Nature* **499,** 316–319 (2013).
12. Tan, Z. *et al.* Bright light-emitting diodes based on organometal halide perovskite. *Nature Nanotechnol.* **9,** 687–692 (2014).
13. Stranks, S. D. *et al.* Electron-hole diffusion lengths exceeding 1 micrometer in an organometal trihalide perovskite absorber. *Science* **342,** 341–344 (2013).
14. Mitzi, D. B., Chondroudis, K. & Kagan, C. R. Organic-inorganic electronics. *IBM J. Res. Dev.* **45,** 29–45 (2001).
15. Ning, Z., Dong, H., Zhang, Q., Voznyy, O. & Sargent, E. H. Solar cells based on inks of n-type colloidal quantum dots. *ACS Nano* **8,** 10321–10327 (2014).
16. Dirin, D. N. *et al.* Lead halide perovskites and other metal halide complexes as inorganic capping ligands for colloidal nanocrystals. *J. Am. Chem. Soc.* **136,** 6550–6553 (2014).
17. Leitsmann, R. *et al.* Adsorption mechanisms of fluorocarbon polymers at ultra low-*k* surfaces. *Surf. Sci.* **604,** 1808–1812 (2010).
18. Koch, C. T. *Determination of Core Structure Periodicity and Point Defect Density along Dislocations*. PhD thesis, Arizona State Univ. (2002).
19. Moroz, P. *et al.* Suppressed carrier scattering in CdS-encapsulated PbS nanocrystal films. *ACS Nano* **7,** 6964–6977 (2013).
20. Gao, Y. *et al.* Enhanced hot-carrier cooling and ultrafast spectral diffusion in strongly coupled PbSe quantum-dot solids. *Nano Lett.* **11,** 5471–5476 (2011).
21. Wise, F. W. Lead salt quantum dots: the limit of strong quantum confinement. *Acc. Chem. Res.* **33,** 773–780 (2000).
22. Choi, J. J. *et al.* Photogenerated exciton dissociation in highly coupled lead salt nanocrystal assemblies. *Nano Lett.* **10,** 1805–1811 (2010).
23. Kagan, C. R., Murray, C. B., Nirmal, M. & Bawendi, M. Electronic energy transfer in CdSe quantum dot solids. *Phys. Rev. Lett.* **76,** 1517–1520 (1996).
24. Xu, F. *et al.* Efficient exciton funneling in cascaded PbS quantum dot superstructures. *ACS Nano* **5,** 9950–9957 (2011).
25. Ponseca, C. S. *et al.* Organometal halide perovskite solar cell materials rationalized: ultrafast charge generation, high and microsecond-long balanced mobilities, and slow recombination. *J. Am. Chem. Soc.* **136,** 5189–5192 (2014).


**Acknowledgements** This publication is based, in part, on work supported by an award (KUS-11-009-21) from the King Abdullah University of Science and Technology (KAUST), by the Ontario Research Fund Research Excellence Program and by the Natural Sciences and Engineering Research Council (NSERC) of Canada. Computations were performed using the BlueGene/Q supercomputer at the SciNet HPC Consortium provided through the Southern Ontario Smart Computing Innovation Platform (SOSCIP). E.Y. acknowledges support from an FAPESP-BEPE (14/18327-9) fellowship. The authors thank L. Levina for assistance in CQD synthesis, E. Beauregard for assistance in PHC synthesis, Z. Yang and M. Adachi for discussions, and E. Palmiano, R. Wolowiec and D. Kopilovic for their help during the course of study.

**Author Contributions** Z.N., X.G., R.C. and E.H.S. designed and directed the study. Z.N. and X.G. contributed to all the experimental work. R.C. carried out the photoluminescence lifetime and excitation measurements and analysis. G.W. and S.H. performed the PLQE and the carrier transfer efficiency study. F.F. and E.Y. did the TEM measurement and FFT analysis. O.V. carried out the TEM simulation and XPS measurement. O.V. and A.B. performed the DFT simulation. Z.N., X.G., R.C., and E.H.S. wrote the manuscript. All authors commented on the paper.

**Author Information** Reprints and permissions information is available at www.nature.com/reprints. The authors declare no competing financial interests. Readers are welcome to comment on the online version of the paper. Correspondence and requests for materials should be addressed to E.H.S. (ted.sargent@utoronto.ca).

## METHODS

**CQD synthesis and solution ligands exchange.** Colloidal quantum dots (CQDs) were synthesized using methods previously reported[26]. For iodide ligand exchange, 3 ml of CQDs dispersed in octane (10 mg ml$^{-1}$) were added into 3 mL of dimethylformamide (DMF) solution containing 350 mg of $PbI_2$ and 150 mg of $CH_3NH_3I$. After stirring for 10 min, CQDs had transferred from the top octane phase to the bottom DMF. After removing the octane, we washed the CQD solution three more times using octane to remove the organic residue. Subsequently, the CQDs were precipitated by the addition of toluene. The nanoparticles were dispersed in butylamine for film fabrication.

**Poly-heterocrystalline (PHC) solids fabrication.** A given amount of $PbI_2$ (with one quarter weight ratio of $CH_3NH_3I$) was added into the solution for perovskite growth. A spin-coating process was used for film fabrication (spin speed of 6,000 r.p.m). The film was then annealed at 70 °C for 10 min in a $N_2$ glovebox. For perovskite growth, methylammonium iodide solution (10 mg ml$^{-1}$ in isopropanol) was dropped and left on the film for 30 s. After removing the solution by spin coating (spin speed 6,000 r.p.m.), the film was soaked in pure isopropanol for 10 s, and then a spin-coating process was performed to remove the residual solvent. Finally, the film was annealed again at 70 °C for 10 min in a $N_2$ glovebox.

**Density functional theory (DFT) simulations.** Calculations were performed within the DFT formalism using a Perdew–Burke–Ernzerhof[27] generalized gradient approximation exchange correlation functional. All calculations were performed using the CP2K[28] package with mixed Gaussian and plane-wave basis set, using the molecularly optimized MOLOPT[28] double ζ-valence polarized (mDZVP) basis set implemented in CP2K code, which has very small basis set superposition errors in gas and condensed phases[17,29–31]. The charge density cut-off was 300 Ry, which is suitable for the Goedecker–Teter–Hutter pseudopotentials[32]. Spin polarized (local-spin-density approximation) and spin-unpolarized calculations (local-density approximation) were performed in the cases of odd and even numbers of electrons, respectively. The structural minimization was performed using a Broyden–Fletcher–Goldfarb–Shanno algorithm[33]. Surface slabs were modelled as (110) $MAPbI_3$ of tetragonal structure and (100) cubic PbS with seven monolayers each. 100 Å of vacuum was added on top of the slab. Dipole correction was used to remove artificial dipole–dipole interaction across periodic images as implemented in the CP2K v2.5. A 3 × 3 (26.88 Å × 26.88 Å) supercell was used in the $X$–$Y$ plane.

The interfacial energy was computed using the relation[34]

$$E_{\text{inter}}^{\text{MAPbI}_3-\text{PbS}} = E_s(\text{MAPbI}_3) + E_s(\text{PbS}) - E_{\text{ad}}(\text{MAPbI}_3-\text{PbS})$$

where $E_s$ represents the surface energies of the corresponding surfaces ($MAPbI_3$ and PbS), and $E_{ad}(MAPbI_3$–PbS) is the adsorption energy of the $MAPbI_3$ on PbS. The interfacial energy describes the energy required to cut the PbS and $MAPbI_3$ bulk and combine the obtained free surfaces to form the MAPbI3–PbS interface.

The estimated surface energy of PbS(100) is 9 meV Å$^{-2}$, which is in close agreement with previously reported[35] values of 12 meV Å$^{-2}$. The $MAPbI_3$ surface energy is[36,37] 9 meV Å$^{-2}$. The adsorption energy is calculated via

$$E_{\text{ad}}(\text{MAPbI}_3-\text{PbS}) = E_{\text{slab}}(\text{MAPbI}_3) + E_{\text{slab}}(\text{PbS}) - E_{\text{slab}}(\text{MAPbI}_3-\text{PbS})$$

where $E_{slab}$ is the slab energy of the corresponding bare $MAPbI_3$ or PbS slab, and $E_{slab}(MAPbI_3$–PbS) is the energy of the combined PbS–$MAPbI_3$ slab. The adsorption energy is calculated to be about 12 meV Å$^{-2}$, which gives a value of the interfacial energy of the order of the 6 meV Å$^{-2}$. The value obtained for the interfacial energy, which is smaller than that of free surfaces, is indicative of the matched interface being favoured over broken bonds at the interface.

Calculations to investigate a PbS CQD embedded in a perovskite matrix were performed using a 50.6 Å$^3$ box that contained about 3,000 atoms. The relaxed lattice constant of the perovskite was imposed on the unit cell, corresponding to approximately 5% tensile strain on PbS. A PbS CQD of about 3 nm in diameter fully relaxed in vacuum was placed inside a manually prepared cavity in perovskite providing an epitaxial matching. Fully quantum mechanical total-energy minimization was performed on the combined system.

We find that the PbS lattice constant is changed by only 0.5% strain, instead of by the imposed 5% difference between its lattice constant and that of the perovskite (Extended Data Fig. 7). The preponderance of the lattice constant change is accommodated in the perovskite in a thin layer within one or two lattice constants near the interface. This can be explained by the fact that PbS is much stiffer than perovskite: the bulk modulus of PbS is $B_{PbS}$ = 53 GPa (ref. 38), whereas for perovskite it is $B_{perovskite}$ = 12.2 GPa (ref. 39). Calculated bandgaps for a strained PbS 3-nm CQD in vacuum are: $E_g$[no strain] = 1.06 eV, and $E_g$[0.5% tensile strain] = 1.08 eV, consistent with deformation potentials derived from temperature dependent bandgaps for these CQD sizes[21].

This bandgap change corresponds to an approximately 24 nm blueshift, consistent with the excess blueshift observed experimentally in low-loading samples that is greater than the shift associated with low dot-to-dot communication.

**Decoupling of perovskite and CQD contribution in TEM.** We used high-angle annular dark-field scanning transmission electron microscopy (HAADF-STEM) to image the dots in perovskite. The corresponding signal, which originates from electrons that are scattered incoherently at large angles, provides contrast between the heavier (denser) CQDs and the lighter $MAPbI_3$ matrix. Under these conditions, contributions from diffraction and phase are suppressed, and the contrast therefore depends mainly on the atomic number $Z$. Consequently, the denser PbS CQDs will scatter electrons more strongly, yielding a higher intensity at the detector than when imaging the perovskite crystal matrix. This contrast is seen in the HAADF-STEM map of a CQD–perovskite thin film with 3.9% CQD loading (Extended Data Fig. 5c), with brighter regions marking the presence of CQDs with diameters of about 5 nm. The absence of these intensity variations in a pure perovskite matrix is shown in Extended Data Fig. 5a, which shows a single perovskite grain (white region) in which no brightness fluctuations are observed. The corresponding HRTEM maps are shown in Extended Data Fig. 5b (pure perovskite film) and the inset of Extended Data Fig. 5c (CQD–perovskite thin film). In the latter, the HRTEM is only acquired in the region highlighted by the yellow circle, which is expanded in Extended Data Fig. 5d to provide a comparison with the HRTEM map shown in Fig. 2g. Notably, the CQDs appear as dark in HRTEM, demonstrating the validity of the framework used for the analysis discussed in the main text.

**Extraction of transport efficiency from PLQE and photoluminescence decay.** We define the total transfer efficiency ($\eta_{tot}$) and diffusion transport efficiency ($\eta_{diff}$) as

$$\eta_{\text{tot}} = \frac{n_{\text{trans}}}{n_{\text{all}}} \quad \text{and} \quad n_{\text{diff}} = \frac{n_{\text{diff}}}{n_{\text{all}}}$$

where $n_{trans}$ is the number of charge carriers that are transferred into the CQDs from the perovskite, $n_{diff}$ is the number of carriers that reach the CQDS by diffusing across the perovskite matrix, and $n_{all}$ is the total number of photogenerated charge carriers in the perovskite.

Experimentally, $\eta_{tot}$ is extracted from photoluminescence quantum efficiency (PLQE) measurement using a modified version of a method reported in the literature[40]. We measured the photoluminescence from CQDs in matrix using two excitation wavelengths: a short wavelength that excites both CQDs and perovskite, and a long wavelength that only excites CQDs. The photoluminescence (PL) of CQDs in these two scenarios are

$$\text{PL}_{\text{CQDs,short}} = \left(A_{\text{CQDs,short}} + \eta_{\text{tot}} A_{\text{p,short}}\right) \times \text{PLQE}_{\text{CQDs}} \times I_{\text{ex,short}} \quad (1)$$

$$\text{PL}_{\text{CQDs,long}} = A_{\text{CQDs,long}} \times \text{PLQE}_{\text{CQDs}} \times I_{\text{ex,long}} \quad (2)$$

$PL_{CQDs}$ and $I_{ex}$ represent the photoluminescence yield from the CQDs (in photons per second) and the photon intensity of the excitation source (in photons per second), respectively. $A_{CQDs}$ and $A_p$ are the absorption of CQDs and perovskite, respectively. $A_{CQDs}$ was determined by measuring the change in absorbance at the dot's excitonic peak and scaling the total material absorbance at the chosen wavelength by this factor. $A_p$ was determined using the additive property of absorbances for a mixture. The Beer–Lambert law was used to convert the experimental absorption measurements to absorbances for use in these calculations. Owing to very low optical density for the absorption of CQDs in films with low CQD concentration, the values of $A_{CQDs}$ were estimated using a linear scaling (according to the CQD concentration), on the basis of the measured $A_{CQDs}$ for a film with 28% CQD concentration (highest loading). The PLQE is calculated using an integrating sphere and following a method described elsewhere[41]. The intensity of the excitation source was measured using a power meter (LaserStar). The wavelength-dependent responses of the visible and near-infrared photon detectors (for photoluminescence and PLQE measurements) were corrected using an Ocean Optics LS-1 calibration lamp with a known spectral profile. The 'short' and 'long' in the subscripts indicate the wavelength regime. From equations (1) and (2), we determine

$$\eta_{\text{tot}} = \left[\left(\frac{\text{PL}_{\text{QDs,short}} \times I_{\text{ex,long}}}{\text{PL}_{\text{QDs,long}} \times I_{\text{ex,short}}}\right) A_{\text{QDs,long}} - A_{\text{QDs,short}}\right] \frac{1}{A_{\text{p,short}}} \quad (3)$$

The CQD photoluminescence scans that are used to extract the total integrated (with respect to wavelength) photoluminescence intensity (normalized with the incident light intensity $I_{ex}$), $PL_{CQDs}/I_{ex}$, are plotted against wavelength in Extended Data Fig. 6c, d. Owing to the presence of a detector cut-off at long wavelength (about 1,380 nm), the integrated area of the left half-peak (shaded area in Extended Data Fig. 6c, d) is evaluated as $\text{PL}_{\text{CQDs}} = \int_{1{,}000\text{nm}}^{\lambda_{\text{peak}}} \text{PL}(\lambda)\text{d}\lambda$ and then doubled to obtain the total photoluminescence. The absorption scans used to extract the absorption

coefficients $A_{CQDs}$ and $A_p$ are plotted in Extended Data Fig. 6e; the results are presented in Extended Data Table 1b.

**Dynamic model for time-resolved photoluminescence.** For the perovskite matrix, by considering bimolecular recombination as the dominant radiative relaxation pathway[42], the photoluminescence intensity of perovskite is

$$I_{PL,p}(t) = k_{rad,p}\left[n_p(t)\right]^2 \quad (4)$$

where $k_{rad,p}$ is the bimolecular recombination rate of perovskite, and $n_p(t)$ is charge carrier density in perovskite, whose time evolution is modelled as arising from two contributions: a fast exponential decay (carriers rapidly transferred to dots) plus a slower radiative decay

$$n_p(t) = a_1 e^{-k_{ct}t} + \frac{1}{k_{rad,p}t + a_2} \quad (5)$$

where $a_1$ and $a_2$ are constants, and $k_{ct}$ is the charge carrier transfer rate, which corresponds to the reciprocal of the average time for a carrier to reach (and get captured by) a CQD via diffusion in the matrix. From equations (4) and (5), the photoluminescence intensity of perovskite is

$$I_{PL,p}(t) = k_{rad,p}\left[a_1 e^{-k_{ct}t} + \frac{1}{k_{rad,p}t + a_2}\right]^2 \quad (6)$$

For CQDs in matrix, both exciton recombination (triggered by the direct excitation of excitons in dots) and bimolecular recombination (due to free carriers injected from the matrix) contribute to photoluminescence:

$$I_{PL,CQDs}(t) = k_{ex\text{-}rad}n_{ex}(t) + k_{rad,CQDs}\left[n_{CQDs}(t)\right]^2 \quad (7)$$

Here, $k_{ex-rad}$ is the exciton radiative recombination rate, $k_{rad,CQDs}$ is the bimolecular recombination rate of free carriers in CQDs, and $n_{ex}$ and $n_{CQDs}(t)$ represent the exciton and injected free carrier density in CQDs, respectively. The exciton density and free carrier density are

$$n_{ex}(t) = n_{ex0}e^{-k_{ex}t} \quad (8)$$

$$n_{CQDs}(t) = \frac{1}{k_1 t + a_3}\left(1 - e^{-k_{ct}t}\right) \quad (9)$$

respectively, where $n_{ex0}$ represents the initial exciton density, $k_{ex}$ and $k_1$ are the total recombination rate of excitons and free charge carrier constants, respectively, and $a_3$ is a constant.

Considering equations (7)–(9), the photoluminescence intensity of CQDs is

$$I_{PL,CQDs}(t) = k_{ex}n_{ex0}e^{-k_{ex}t} + k_{rad,CQDs}\left[\frac{1}{k_1 t + a_3}\left(1 - e^{-k_{ct}t}\right)\right]^2 \quad (10)$$

The models given in equations (6) and (10) are used to fit the photoluminescence decay traces of CQDs and perovskite and extract the parameters that are most relevant for charge transport, loss, and recombination across the film.

Extended Data Fig. 10 shows the integrated (with respect to time) photoluminescence from the exciton term in equation (10)

$$\widetilde{PL}_{ex} = \int k_{ex}n_{ex0}e^{-k_{ex}t}dt$$

as well as the integrated (with respect to time) photoluminescence from free carrier recombination term in equation (10)

$$\widetilde{PL}_{ca} = \int k_{rad,CQDs}\left[\frac{1}{k_1 t + a_3}\left(1 - e^{-k_{ct}t}\right)\right]^2 dt$$

**Estimate of carrier diffusion length in perovskite matrix.** In general, the diffusion length $L_D$ of carriers in any material may be calculated from the diffusion coefficient $D$ and the carrier lifetime $\tau$ using

$$L_D = \sqrt{D\tau} \quad (11)$$

Using the experimentally determined carrier lifetime in the perovskite matrix (evaluated from the decay time of the perovskite photoluminescence emission; see Fig. 4d), we estimate the diffusion length for carriers in our PHC films for possible values of the diffusion coefficient (which cannot be directly measured) in the range previously determined in pure lead iodide perovskite films[13]. The corresponding data points for $L_D$ as a function of CQD volume concentration are shown in Extended Data Fig. 9. This figure shows that the estimated values for $L_D$ are comparable to the calculated average inter-dot spacing (red line), which suggests that the diffusion length in the matrix is ultimately determined by the average free space available for carriers to diffuse in the matrix before being transferred to the CQDs.

**Code availability.** CP2K is freely available from http://www.cp2k.org/.


26. Hines, M. A. & Scholes, G. D. Colloidal PbS nanocrystals with size-tunable near-infrared emission: observation of post-synthesis self-narrowing of the particle size distribution. *Adv. Mater.* **15,** 1844–1849 (2003).
27. Perdew, J. P., Burke, K. & Ernzerhof, M. Generalized gradient approximation made simple. *Phys. Rev. Lett.* **77,** 3865–3868 (1996).
28. VandeVondele, J. & Hutter, J. Gaussian basis sets for accurate calculations on molecular systems in gas and condensed phases. *J. Chem. Phys.* **127,** 114105 (2007).
29. Takaluoma, T. T., Laasonen, K. & Laitinen, R. S. Molecular dynamics simulation of the solid-state topochemical polymerization of $S_2N_2$. *Inorg. Chem.* **52,** 4648–4657 (2013).
30. Bork, N., Loukonen, V. & Vehkamki, H. Reactions and reaction rate of atmospheric $SO_2$ and $O^-_3(H_2O)_n$ collisions via molecular dynamics simulations. *J. Phys. Chem. A* **117,** 3143–3148 (2013).
31. Smecca, E., Motta, A., Fragal, M. E., Aleeva, Y. & Condorelli, G. G. Spectroscopic and theoretical study of the grafting modes of phosphonic acids on ZnO nanorods. *J. Phys. Chem. C* **117,** 5364–5372 (2013).
32. Hartwigsen, C., Goedecker, S. & Hutter, J. Relativistic separable dual-space Gaussian pseudopotentials from H to Rn. *Phys. Rev. B* **58,** 3641–3662 (1998).
33. Press, W. H., Teukolsky, S. A., Vetterling, W. T. & Flannery, B. P. *Numerical Recipes: The Art of Scientific Computing* 3rd edn, Ch. 10.9 (Cambridge Univ. Press, 2007).
34. Liu, W., Li, J. C., Zheng, W. T. & Jiang, Q. Ni Al (110)/Cr (110) interface: a density functional theory study. *Phys. Rev. B* **73,** 205421 (2006).
35. Zherebetskyy, D. *et al.* Hydroxylation of the surface of PbS nanocrystals passivated with oleic acid. *Science* **344,** 1380–1384 (2014).
36. Buin, A. *et al.* Materials processing routes to trap-free halide perovskites. *Nano Lett.* **14,** 6281–6286 (2014).
37. Haruyama, J., Sodeyama, K., Han, L. & Tateyama, Y. Termination dependence of tetragonal $CH_3NH_3PbI_3$ surfaces for perovskite solar cells. *J. Phys. Chem. Lett.* **5,** 2903–2909 (2014).
38. Bian, K., Bassett, W., Wang, Z. & Hanrath, T. The strongest particle: size-dependent elastic strength and Debye temperature of PbS nanocrystals. *J. Phys. Chem. Lett.* **5,** 3688–3693 (2014).
39. Feng, J. Mechanical properties of hybrid organic-inorganic $CH_3NH_3BX_3$ (B = Sn, Pb; X = Br, I) perovskites for solar cell absorbers. *APL Mat.* **2,** 081801 (2014).
40. Tikhomirov, G. *et al.* DNA-based programming of quantum dot valency, self-assembly and luminescence. *Nature Nanotechnol.* **6,** 485–490 (2011).
41. de Mello, J. C., Wittmann, H. F. & Friend, R. H. An improved experimental determination of external photoluminescence quantum efficiency. *Adv. Mater.* **9,** 230–232 (1997).
42. Manser, J. S. & Kamat, P. V. Band filling with free charge carriers in organometal halide perovskites. *Nature Photon.* **8,** 737–743 (2014).

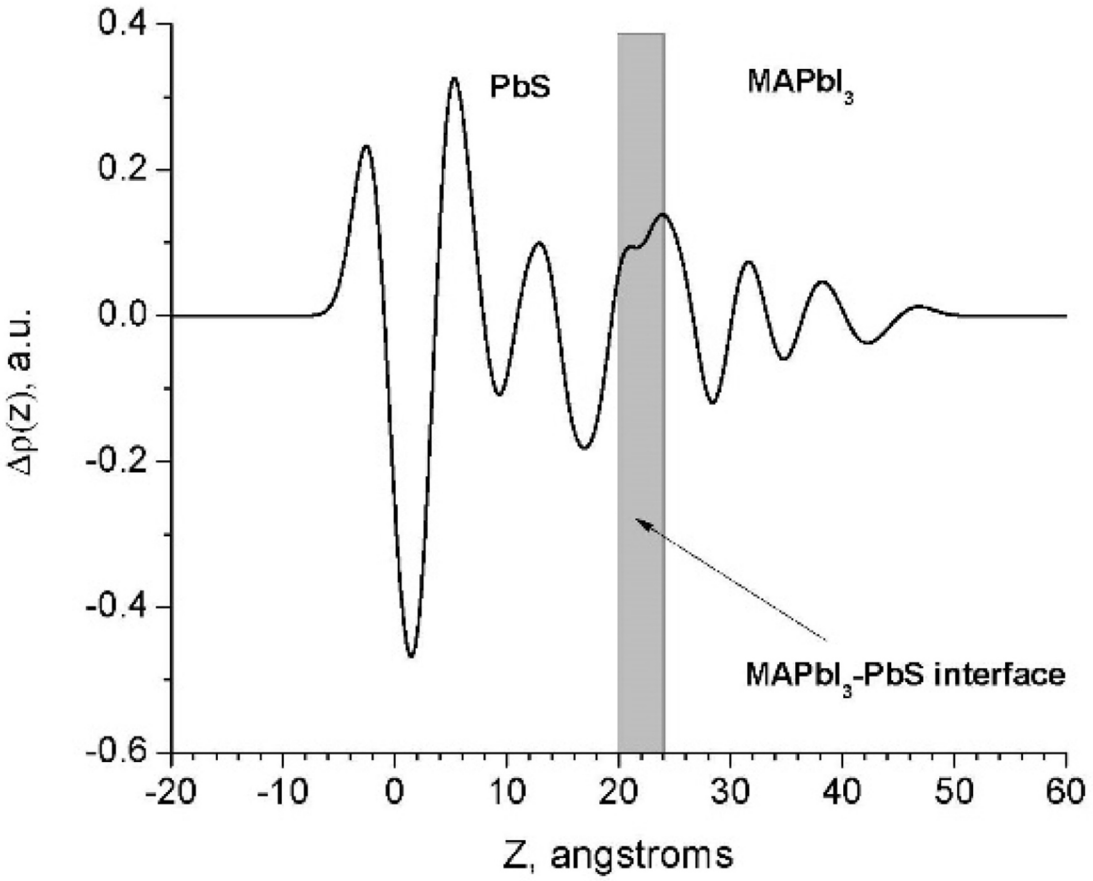


**Extended Data Figure 1 | Planar averaged total charge difference with respect to the pristine slabs.** The total charge difference ($\Delta\rho$) is measured along the $Z$ axis of the material.

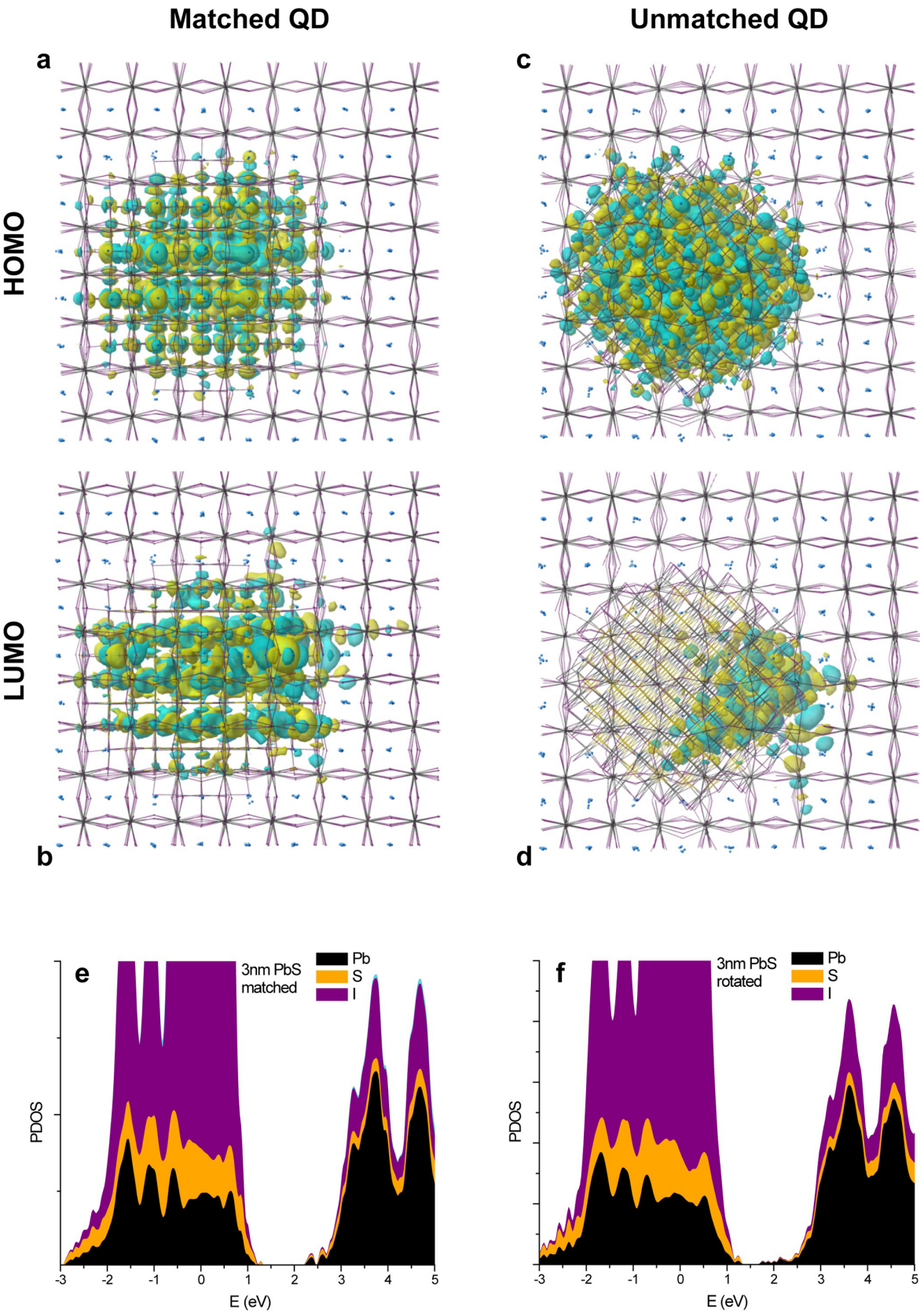


**Extended Data Figure 2 | DFT simulation.** **a**, **b**, Highest occupied molecular orbital (HOMO) and lowest unoccupied molecular orbital (LUMO), respectively, of a matched CQD. **c**, **d**, HOMO and LUMO, respectively, of mismatched dots. The states are mostly localized within the CQD in matched dots, whereas they are localized on the interface between the CQDs and perovskite in mismatched dots, indicating the formation of defects in the latter. **e**, **f**, The projected density of states (PDOS) as a function of energy (*E*) of matched and mismatched (rotated) CQDs, respectively.

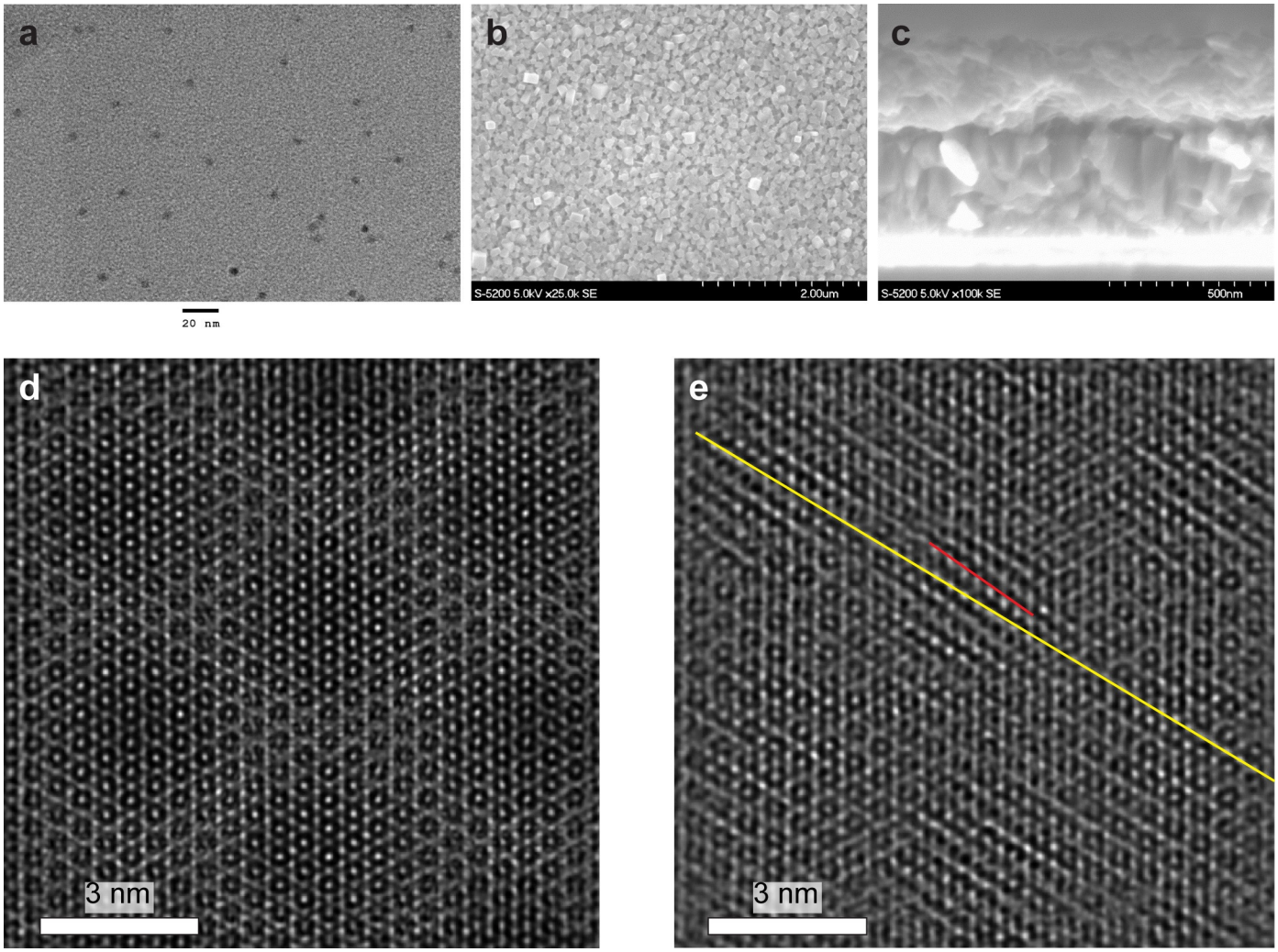


**Extended Data Figure 3 | Microscopic images.** **a**, TEM image of CQDs after solution-phase iodide–ligands exchange. The average CQD size is approximately 4 nm. **b**, Scanning electron microscopy (SEM) image of the film surface with CQDs embedded in perovskite matrix (CQD volume percentage of 3.8%). The average perovskite grain size is about 60 nm. **c**, SEM image of the cross-section of the film with CQDs embedded in perovskite matrix (CQD volume percentage of 3.8%). The film thickness is about 240 nm (top layer). **d**, **e**, Simulated TEM images of matched (**d**) and mismatched (**e**) CQDs and perovskite. Yellow line, perovskite lattice plane; red line, CQD lattice plane.

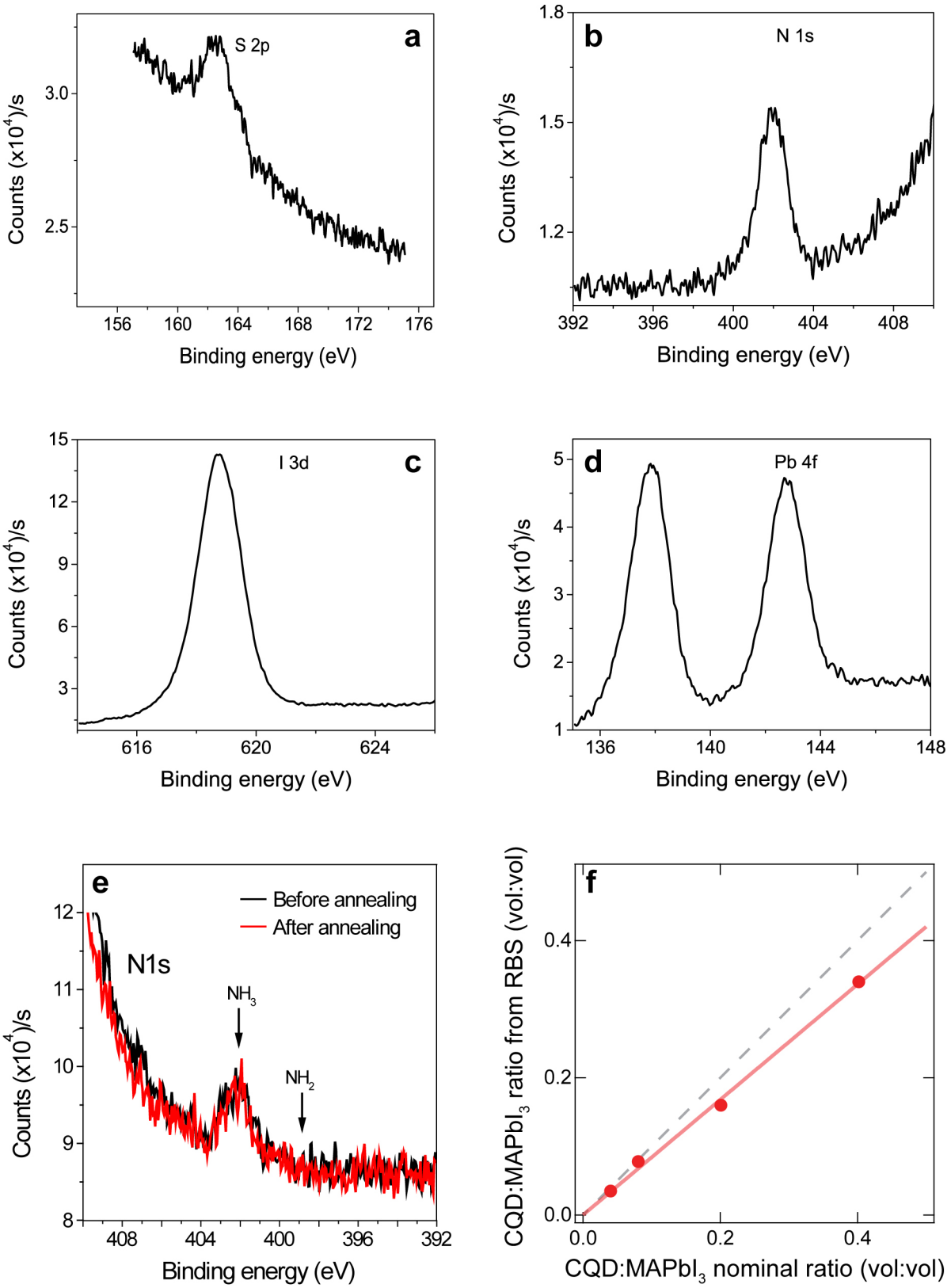


**Extended Data Figure 4 | Compositional analysis of PHC. a–d**, XPS analysis of the CQDs embedded in PHC film (Pb 4*f*, S 2*p*, N 1*s*, I 3*d*). All the elements (as labelled) are observed in the film, indicating the existence of both PbS and $MAPbI_3$. **e**, XPS spectra of the N 1*s* orbital for high-loading PbS films, which follows the ligand exchange to perovskite ligands in butylamine, before and after annealing at 70 °C for 10 minutes, before the methylammonium post-treatment step. We detect only the ammonium signal at 402 eV and no amine signal at 398–399 eV, which suggests that the methylammonium iodide ligand is more stable on the surface and displaces weakly bound buylamine, even before film annealing. **f**, Plot of the nominal volume ratio of CQDs to perovskite versus the ratio measured using RBS (both with the perovskite value scaled to one), with a linear fit (red line) superimposed. The ideal case, where the measured ratio and the nominal ratio are equal, is indicated by the dashed grey line, showing the agreement between the nominal value and the one evaluated using RBS.

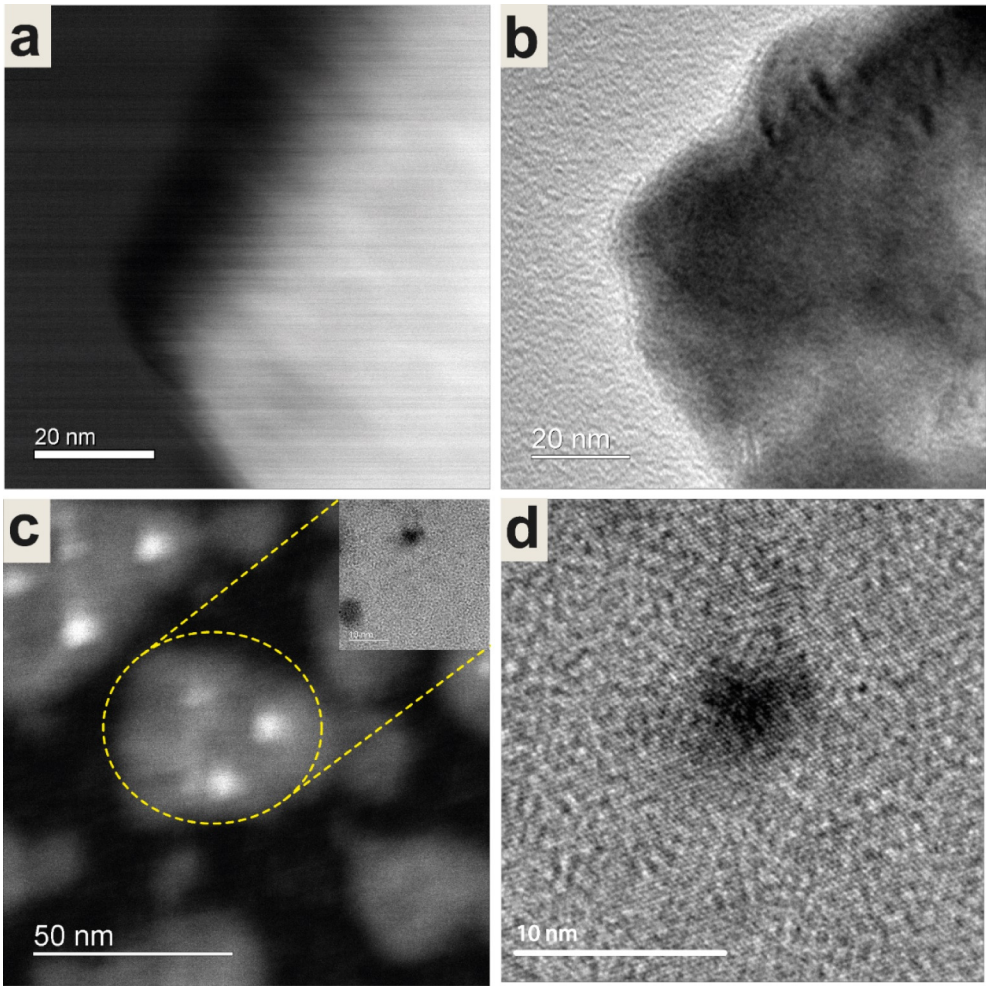


**Extended Data Figure 5 | TEM images of PHC.** **a**, **b**, HAADF-STEM and TEM images of pure perovskite, respectively. **c**, HAADF-STEM image of dots in perovskite. The region indicated by the dashed yellow circle contains three PbS nanocrystals (white spots) located inside perovskite crystal (grey area). Inset, TEM image of part of this region. **d**, A close up of part of the inset in **c**.

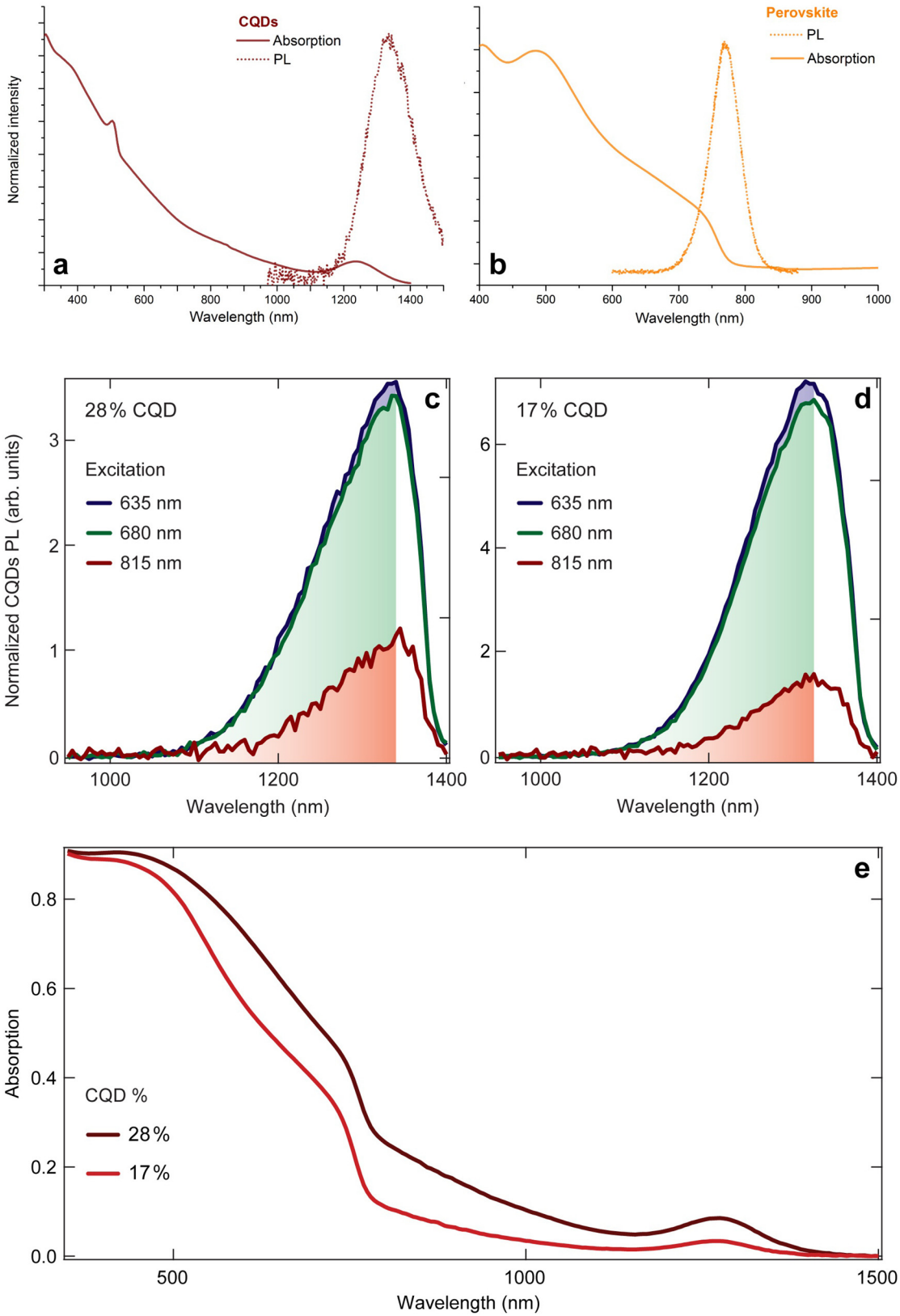


**Extended Data Figure 6 | Absorption and photoluminescence properties of PHC.** **a**, **b**, Absorption and photoluminescence (PL) spectra for a pure CQD film (**a**) and a pure perovskite film (**b**). **c**, **d**, CQD photoluminescence signal from PHC films with 28% (**c**) and 17% (**d**) CQD concentration, acquired at $\lambda = 635$ nm (blue), 680 nm (green), and 815 nm (red). The photoluminescence signal has been normalized by the excitation intensity at the different wavelengths used. The shaded area corresponds the region of the spectrum used to calculate the photoluminescence integrated area in equation (3). **e**, Corresponding optical absorption spectra for a CQD concentration of 28% (dark red) and 17% (red) that were used to evaluate the absorption parameters in, for example, equation (3).

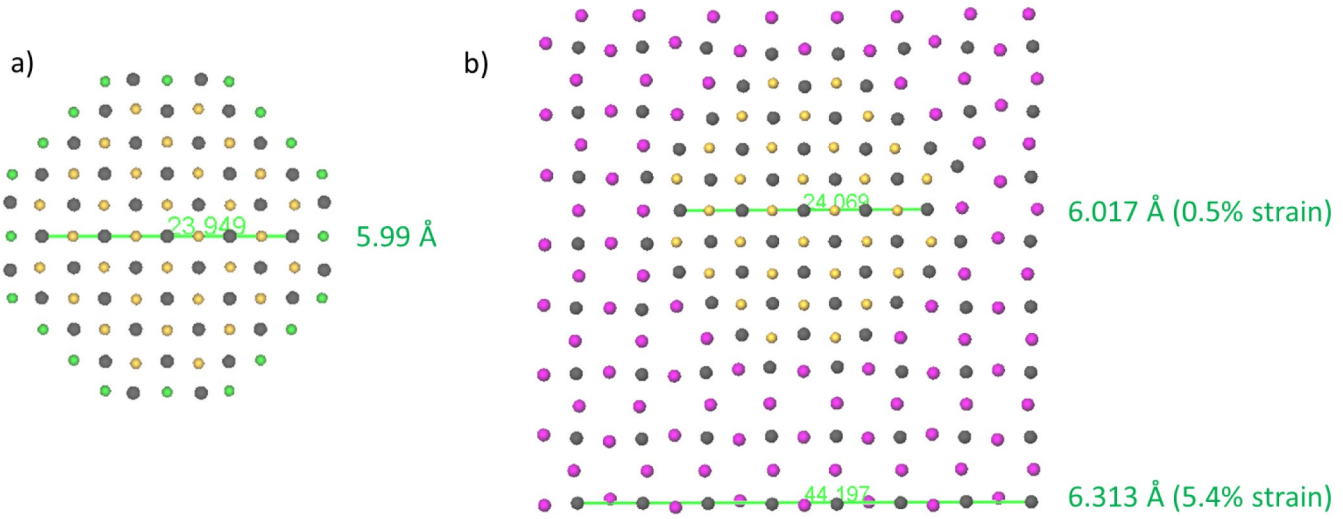


**Extended Data Figure 7 | DFT simulation of strain distribution in PHC composite material.** **a**, Cross-section of the relaxed 3-nm PbS CQD in vacuum. **b**, DFT-optimized geometry of the same 3-nm CQD epitaxially matched with perovskite in a unit cell corresponding to unstrained perovskite. Colours represent the following: grey, lead; yellow and green, sulphur; pink, iodine. The green lines and corresponding numbers are the long-range Pb-to-Pb distance (23.949 Å, 24.069 Å and 44.197 Å); the large green numbers are the average lattice constant (average distance between lead atoms), along those lines.

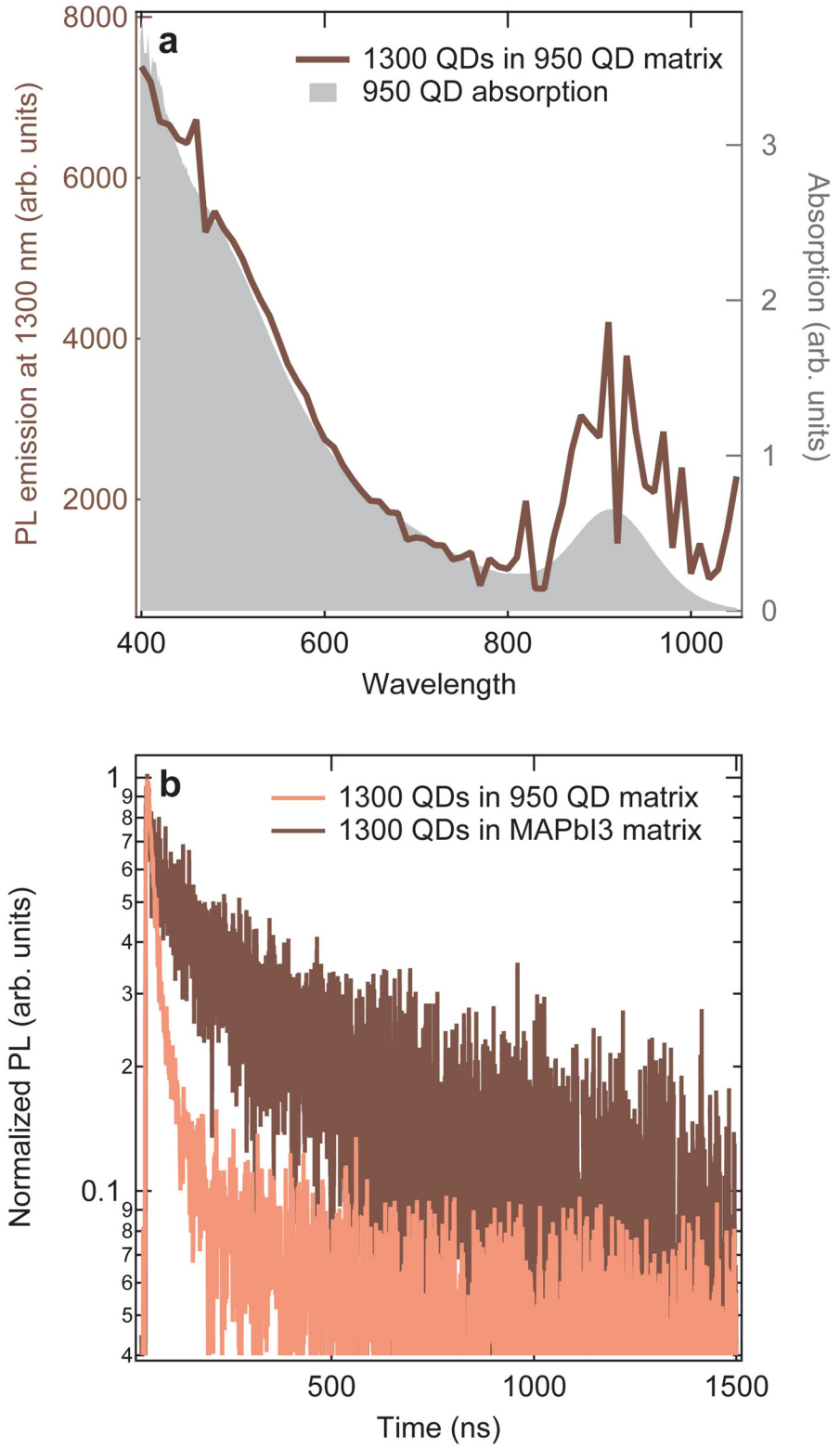


**Extended Data Figure 8 | Photophysical dynamics of CQD-only PHC.** **a**, Photoluminescence (PL) excitation profile from a hybrid film of 1,300-nm-emission CQDs dispersed in 950-nm-emission CQDs (1:10 volume ratio, 'dots-in-dots'), acquired by measuring the photoluminescence emission (at $\lambda \approx 1{,}300$ nm) from the small-bandgap CQDs (1,300-nm-emission CQDs) as a function of excitation wavelength. The absorption profile from the large-bandgap CQDs (950-nm-emission CQDs) is overlaid as the shaded grey area, and exhibits the characteristic excitonic peak at $\lambda \approx 950$ nm. The wavelength dependence of the photoluminescence intensity from the small-bandgap CQDs closely follows the absorption profile of the large-bandgap CQDs, analogous to the dots-in-perovskite films (see Fig. 4b), and is therefore suggestive of carrier funnelling from the large- to the small-bandgap dots. **b**, Photoluminescence decay for 1,300-nm-bandgap CQDs in a CQD-based matrix (light red) and in a perovskite ($MAPbI_3$) matrix (dark red), with 632 nm excitation. The longer dynamics for the CQDs embedded in the perovskite matrix (approximately 150 ns) compared to those for the 'dots-in-dots' (approximately 30 ns) provides evidence for a better passivation of CQDs in the former.

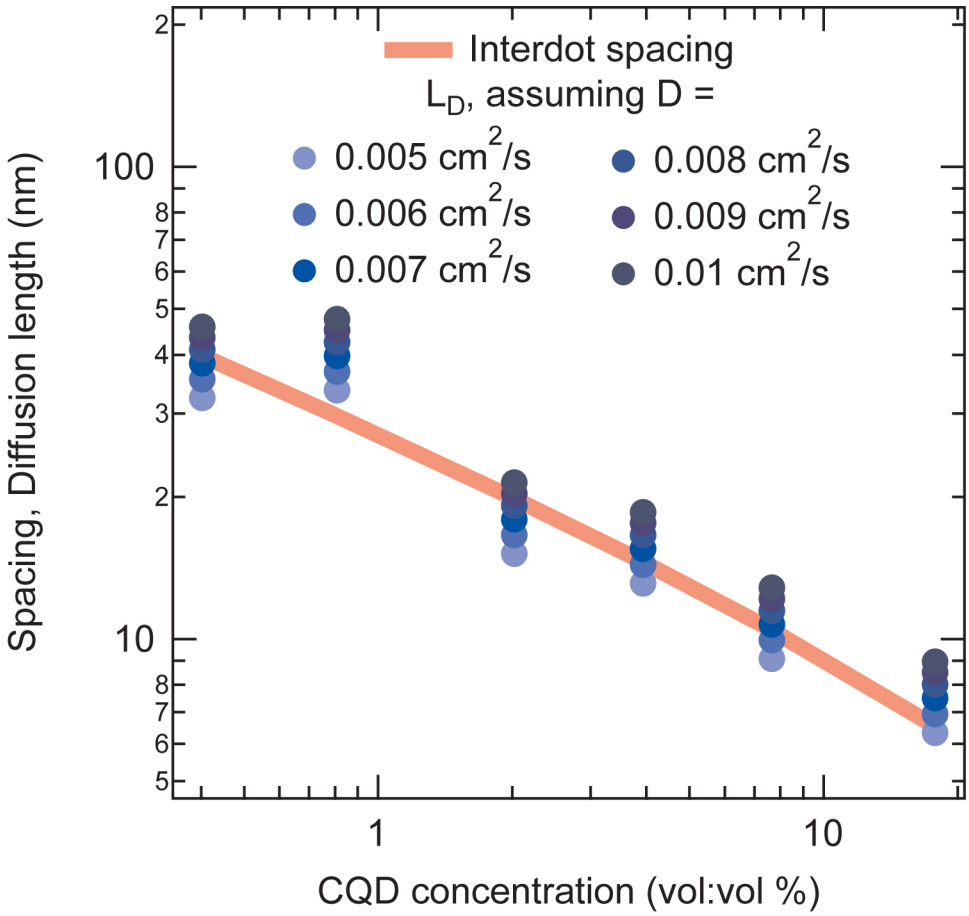


**Extended Data Figure 9 | CQD-concentration-dependent diffusion length.** Plot of the diffusion length $L_D$ of carriers in the perovskite matrix (round markers) for various CQD concentrations, calculated using equation (11) and different possible values for the diffusion coefficient $D$, as labelled. The red line shows the calculated average inter-dot spacing as a function of CQD:$MAPbI_3$ volume ratio.

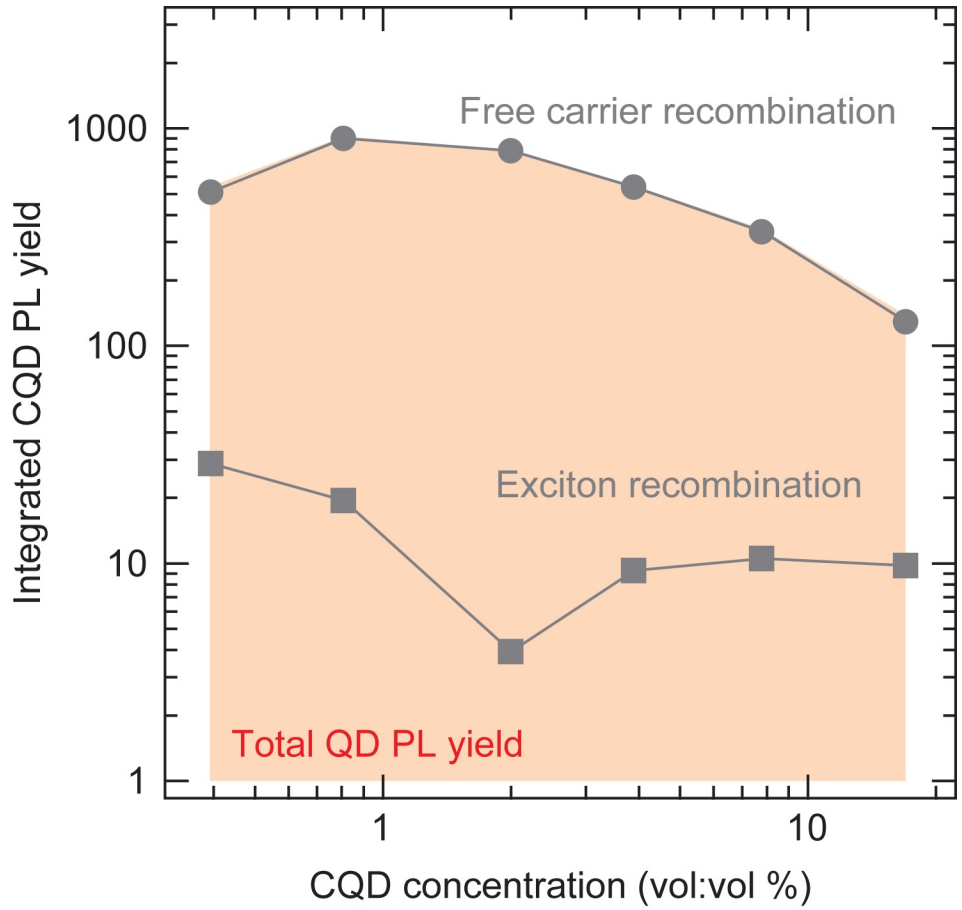


**Extended Data Figure 10 | Integrated photoluminescence contributions of the CQDs.** A stacked plot showing the total photoluminescence yield of the CQDs (shaded area), which is made up of contributions from free carrier recombination and exciton recombination: filled circles represent the integrated (with respect to time) photoluminescence (PL) contribution as a result of free carriers injected from the perovskite ('free carrier recombination'); filled squares represent the integrated (with respect to time) photoluminescence as a result of the dissociation of excitons generated directly in the CQDs ('excitation recombination'); see also equation (10). Consistent with the photoluminescence excitation spectra, the largest contribution to the CQDs photoluminescence is ascribed to radiative recombination of free carriers transferred from the perovskite.

**Extended Data Table 1 | Composition and photophysical parameters of quantum-dot-in-perovskite solid.**

a

| $PbI_2$: PbS Mass:Mass ratio | $MAPbI_3$ : PbS Vol:Vol ratio | PbS : $MAPbI_3$ Vol:Vol ratio | PbS Volume percentage (%) | PbS : $MAPbI_3$ Vol:Volume ratio from fit to RBS |
|---|---|---|---|---|
| 200 | 497.676 | 0.00201 | 0.20053 | 0.00169 |
| 100 | 248.838 | 0.00402 | 0.40026 | 0.00338 |
| 50 | 124.419 | 0.00804 | 0.79733 | 0.00676 |
| 20 | 49.7676 | 0.02009 | 1.96976 | 0.01689 |
| 10 | 24.8838 | 0.04019 | 3.86342 | 0.03378 |
| 5 | 12.4419 | 0.08037 | 7.43942 | 0.06755 |
| 4 | 9.95352 | 0.10047 | 9.12949 | 0.08444 |
| 3 | 7.46514 | 0.13396 | 11.81315 | 0.11259 |
| 2 | 4.97676 | 0.20093 | 16.73147 | 0.16888 |
| 1 | 2.48838 | 0.40187 | 28.6666 | 0.33777 |

b

| CQD Concentration | PL_QDs, short | PL_QDs long | I_ex, short | I_ex, long | A_QDs, long | A_QDs short | A_P, short | Transfer Efficiency |
|---|---|---|---|---|---|---|---|---|
| (vol:vol) | Counts | Counts | Counts | Counts | | | | % |
| 0.004002594 | 10553400 | 476450 | 2378155940 | 872728455 | 0.008 | 0.0220 | 0.351 | 12.55 |
| 0.007973274 | 6152760 | 448548 | 3203109586 | 1321620214 | 0.005 | 0.0103 | 0.396 | 4.97 |
| 0.019697602 | 11752660 | 838076 | 2378155940 | 872728455 | 0.011 | 0.0254 | 0.347 | 9.33 |
| 0.038634204 | 4893860 | 475011 | 3203109586 | 1321620214 | 0.015 | 0.0323 | 0.385 | 8.21 |
| 0.074394245 | 11586780 | 1175544 | 3203109586 | 1321620214 | 0.023 | 0.0492 | 0.368 | 12.03 |
| 0.091294853 | 13070740 | 1359321 | 3203109586 | 1321620214 | 0.024 | 0.0508 | 0.391 | 11.11 |
| 0.118131537 | 4870700 | 586011 | 3203109586 | 1321620214 | 0.080 | 0.1327 | 0.342 | 40.95 |
| 0.167314732 | 3940820 | 307583 | 3203109586 | 1321620214 | 0.067 | 0.1126 | 0.355 | 68.42 |
| 0.286666017 | 2239240 | 256204 | 3203109586 | 1321620214 | 0.164 | 0.2652 | 0.407 | 80.37 |

**a**, List of the values for the nominal $MAPbI_3$ to PbS mass ratio (first column, PbS mass scaled to one) and volume ratio (second column, PbS volume scaled to one), PbS to $MAPbI_3$ volume ratio (third column, reciprocal of second column), and PbS volume as a percentage of the total volume (fourth column). The experimental values for the PbS volume as a percentage of the total volume, as extrapolated from a fit to the RBS data (see also Extended Data Fig. 4) are shown in the fifth column. **b**, Numerical values of the photophysical parameters in equations (1)–(3) that lead to the evaluation of the total (carrier) transfer efficiency $\eta_{tot}$.